Journal of Alloys and Compounds 991 (2024) 174484

Contents lists available at ScienceDirect

Journal of Alloys and Compounds

journal homepage: www.elsevier.com/locate/jalcom

Graphitized carbon nanosheets doped with phosphorus heteroatoms and molybdenum phosphide nanoparticles: A novel cathodic catalyst for fuel cell applications

Vy Anh Tran [a,*], Thu-Thao Thi Vo [b], Van Dat Doan [c], L.M. Nguyen [d], H. Van Tran [e], Van Thuan Le [f,*]

[a] Institute of Applied Technology and Sustainable Development, Nguyen Tat Thanh University, Ho Chi Minh 70000, Viet Nam
[b] Department of Food Science and Biotechnology, Gachon University, 1342 Seongnamdaero, Sujeong-gu, Seongnam-si 13120, Republic of Korea
[c] Faculty of Chemical Engineering, Industrial University of Ho Chi Minh City, Ho Chi Minh, Viet Nam
[d] Faculty of Pharmacy, Thanh Do University, Kim Chung, Hoai Duc, Hanoi 10000, Vietnam
[e] School of Mechanical Engineering, Hanoi University of Science and Technology, No. 1 Dai Co Viet Street, Hanoi 100000, Viet Nam
[f] Center for Advanced Chemistry, Institute of Research and Development, Duy Tan University, 03 Quang Trung, Da Nang 550000, Viet Nam

ARTICLE INFO

Keywords:
Electrocatalyst
Molybdenum phosphide nanoparticles
Phosphorus-doped carbon layer
Oxygen reduction reaction

ABSTRACT

High-efficiency catalysts are required for the oxygen reduction reaction (ORR) in fuel cell applications. Herein, we present a novel hybrid material that is based on uniformly deposited nanoscale molybdenum phosphide (Mo_xP_y) nanoparticles on the structure of graphene nanolayers doped with phosphorus atoms (PG). With a positive onset potential of only −0.046 V and a half-wave potential value of roughly −0.17 V (vs. Ag/AgCl), the obtained hybrid showed good catalytic activity for ORR in 0.1 M KOH electrolyte. It also demonstrated remarkable durability for oxygen reduction reaction in 0.1 M KOH electrolyte when compared to state-of-the-art Pt/C material. The excellent ORR performance can be correlated to the development of a highly conducting microporous structure with highly active sites, which in turn encourages optimal adsorption of intermediates during the ORR process and thus enhances the catalytic process. This work can open a new path for the growth of promising highly efficient catalysts for affordable fuel cell applications.

1. Introduction

The ever-increasing request for sources of fossil fuels along with their critical negative impact on the environment has forced us to find new energy sources such as renewable energy. In this scope, energy conversion techniques like fuel cells have been believed to be an efficient prospect for generating daily energy needed from renewable energy sources [1–3]. However, the cathodic slow oxygen reduction reaction (ORR) hinders the overall energy conversion process, thus increasing the cost of the technique. Therefore, it is required to have immediate attention for the development of low-cost catalysts. Though noble metal-based materials like Pt-based catalysts have been utilized as one of the efficient catalysts for ORR, however, the high cost and insufficient stability impede their use for long-term commercial purposes [4,5]. Therefore, affordable and effective catalysts are highly desirable for ORR standards.

In recent time, a wide range of nonprecious metal materials, including metal hydroxide, metal chalcogenides, metal phosphides, and metal nitrides have been considered as possible alternative catalysts [6–8]. Among these, metal phosphides are believed to be one of the best catalysts because of their unique crystal structure and optimal electronic properties for electrocatalysis [9,10]. In addition, metal phosphides have been used as a favorable ORR catalyst with high activity and outstanding stability [5]. In particular, Mo phosphide material is emerging as a potential candidate as it shows metallic behavior with excellent electronic conductivity and high thermal stability [11]. In addition, less metal-H interaction for these materials because of Mo-P bonds [12–15] lowers the activation energy and thus the overpotential of the catalysis process [16,17]. Nevertheless, the catalytic performance of a bulk phosphide catalyst is relatively inferior in contrast to the noble metal catalysts, because of their low surface area and poor stability during the catalytic process [18,19]. Some studies have demonstrated

* Corresponding authors.
E-mail addresses: tavy@ntt.edu.vn (V.A. Tran), levanthuan3@duytan.edu.vn (V.T. Le).

https://doi.org/10.1016/j.jallcom.2024.174484
Received 27 January 2024; Received in revised form 22 March 2024; Accepted 10 April 2024
Available online 16 April 2024

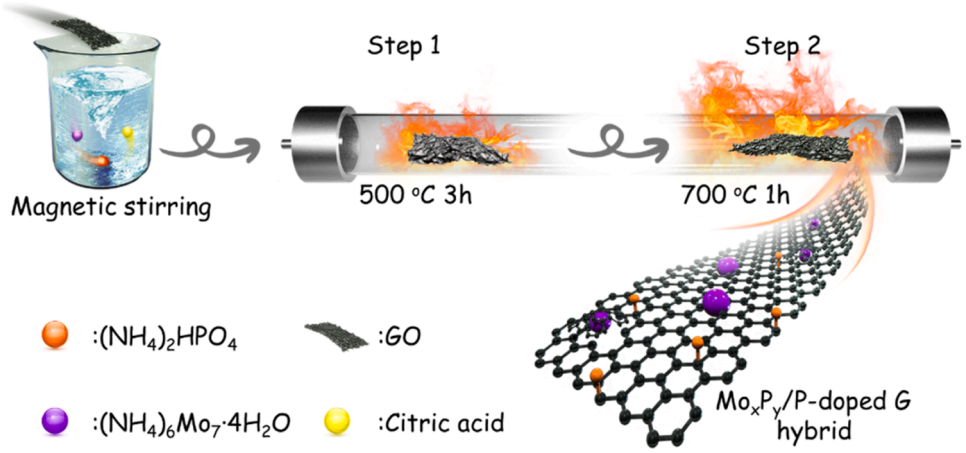

Fig. 1. Schematic demonstration for the development of Mo_xP_y-PG NSs hybrid material.

the distribution of active metal catalysts over the matrix of a carbon support material that holds significant promise for various energy applications [20–22]. For instance, the deposition of catalyst on the graphene (Gr) surface facilitates the enhancement of the active site numbers, promotes charge transfer, and increases material stability [23–26]. Particularly, heteroatom doped Gr catalysts have further evidenced to have better performance not only as an effective support but also an excellent catalyst for electrocatalytic oxygen reduction, caused by its fine-tuning features, such as large area, more active centers, and high charge conductivity [27–30]. Moreover, the distinctive n-type features, characterized by enhanced electron donation, hold significant importance in various catalytic reactions like the reaction of oxygen reduction [31].

Expired by the advantages derived from metal phosphides along with heteroatom-doped Gr layers, in this work, we report a new spongy hybrid structure of uniform Mo phosphide small nanoparticles dispersed on PG nanosheets. The resultant material uplifted the performance for ORR reaction in an alkaline medium by unique nano-engineering along with increased active sites, easy charge transport capabilities, and a flexible network for ion diffusion.

2. Experimental

2.1. Chemical reagents

Potassium permanganate ($KMnO_4$), ammonium hydrogen phosphate ($(NH_4)_2HPO_4$), ammonium molybdate tetrahydrate ($(NH_4)_6Mo_7O_{24}.4\ H_2O$), graphite powder, hydrogen peroxide (H_2O_2), citric acid ($C_6H_8O_7$), and solution of Nafion polymer (5%) were offered by Sigma-Aldrich Co. Sodium carbonate (Na_2CO_3, 99%), potassium hydroxides (KOH, $\geq$ 99.5%), hydrochloric acid (HCl, 35–37%), ethanol (C_2H_5OH, 99.9%), sulfuric acid (H_2SO_4, 99%), and methanol (CH_3OH, 99.9%) were provided by Shanghai Jiahealthy Technology Co. Ltd (China).

2.2. Development of Mo_xP_y-PG NSs hybrid material

Graphene oxide (GO) was synthesized using a specific modified Hummer route [32]. Before creating the Mo_xP_y-PG hybrid material, a solution was prepared through the dispersion of 60 mg of graphene oxide (GO), 9 mg of ammonium hydrogen phosphate, and 0.02 g of $C_6H_8O_7$ in 60 mL of water in a magnetic stirrer for 1 hour. Subsequently, a quantity of 7 milligrams of $(NH_4)_2HPO_4$ was introduced into the solution while maintaining continuous stirring for 5 hours. The resulting mixture was subjected to freeze-drying, resulting in the formation of a solid powder which was subsequently transferred to a quartz glass container placed at the center of an oven to undergo a peculiar calcination procedure. Initially, a calcination process was done at 500 °C in an argon (Ar) atmosphere for 3 hours, utilizing a heating rate of 5°C per minute. This was followed by a subsequent calcination step at 700°C in a hydrogen (H_2) atmosphere for 1 hour, with a warm-up rate of 3 °C per minute. Finally, the temperature of the system was cooled down to ambient conditions and a final powder product was used for subsequent experiments. Fig. 1 shows the process employed in synthesizing the hybrid material of Mo_xP_y-PG.

2.3. Characterization

The morphological characterization of the hybrid catalyst involved scanning electron microscopy (SEM) with a JSM 6600 instrument and transmission electron microscopy (TEM) using a JEM-1400 Philips microscope. Specific surface area measurements were conducted using the SA-9600 Series (HORIBA Co., Japan). The electrochemical properties of the synthesized catalysts were checked by a single-channel potentiostat Biologic SP-200 system (ST Instruments Co., Netherland) intergrated with a three-electrode electrochemical cell, in which the reference electrode, counter electrode, and working electrode were Ag/AgCl (3.0 M KCl), Pt wire, and rotation disk electrode (RDE, disk diameter of 3 mm, purchased from BioLogic Co., France) deposited with the synthesized material, respectively. For preparing the working electrode, 2 mg of the synthesized catalyst was dispersed in 1 mL water/ethanol solvent by sonication for 30 min to form an ink solution. After that, 10 microliters of the ink solution was dropped on surface of the RDE followed by drying at room temperature for 5 h before it was used for electrochemical measurements. The ORR activity and stability of the synthesized materials were evaluated by linear sweep voltammetry (LSV) at different rotation rates of RDE and chronoamperometry (CA) technique. The charge conductivity was measured by electrochemical impedance spectroscopy (EIS) conducted within a frequency range spanning from 10^5 to 10^{-2} Hz. We utilized the Koutecky–Levich (K–L) curve (J^{-1} *vs.* $\omega^{-1/2}$) for determining charge transfer number (n) [33]:

$$\frac{1}{J} = \frac{1}{j_L} + \frac{1}{j_K} = \frac{1}{B\omega^{1/2}} + \frac{1}{j_K} \quad (1)$$

$$B = 0.62nFC_0D_0^{2/3}v^{-1/6} \quad (2)$$

Where, I, I_L, and I_K denote current density response, limiting current density and kinetic diffusion-limiting current density, respectively; ω is the angular velocity of the RDE (rad s^{-1}); C_0 is known as saturated oxygen concentration of 1.2×10^{-3} mol L^{-1} in 0.1 M KOH; D_0 is the oxygen diffusion coefficient of 1.9×10^{-5} cm^2 s^{-1}); ν is the kinetic electrolyte viscosity (0.01 cm^2 s^{-1}), and F is noted as the Faraday

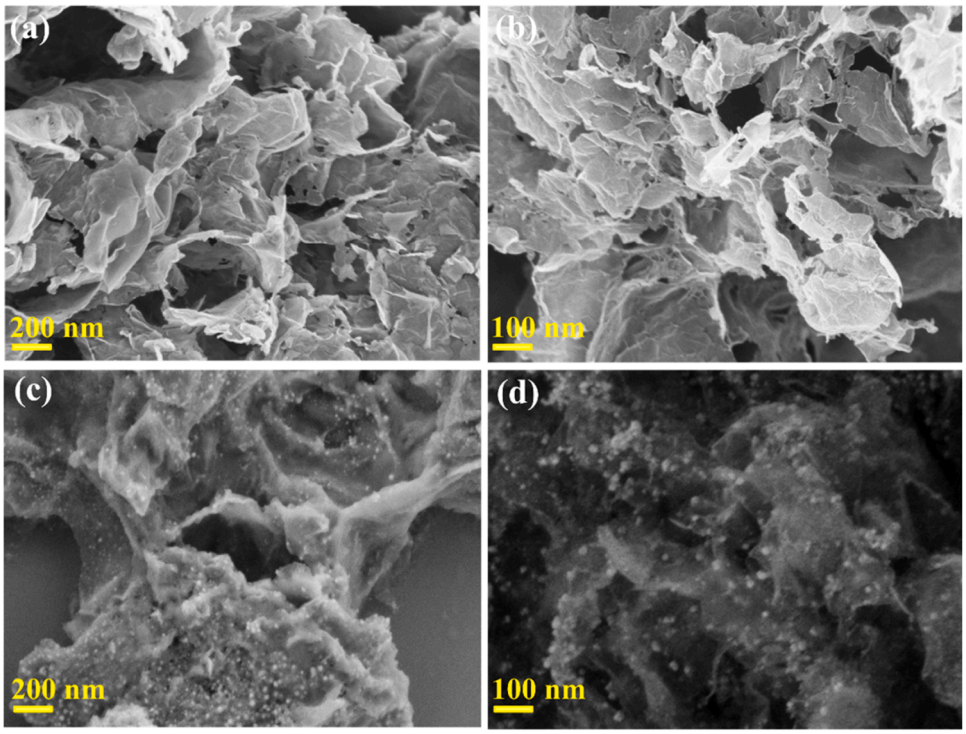

Fig. 2. SEM imageries derived from (a and b) PG together with (c and d) Mo_xP_y-PG hybrid material.

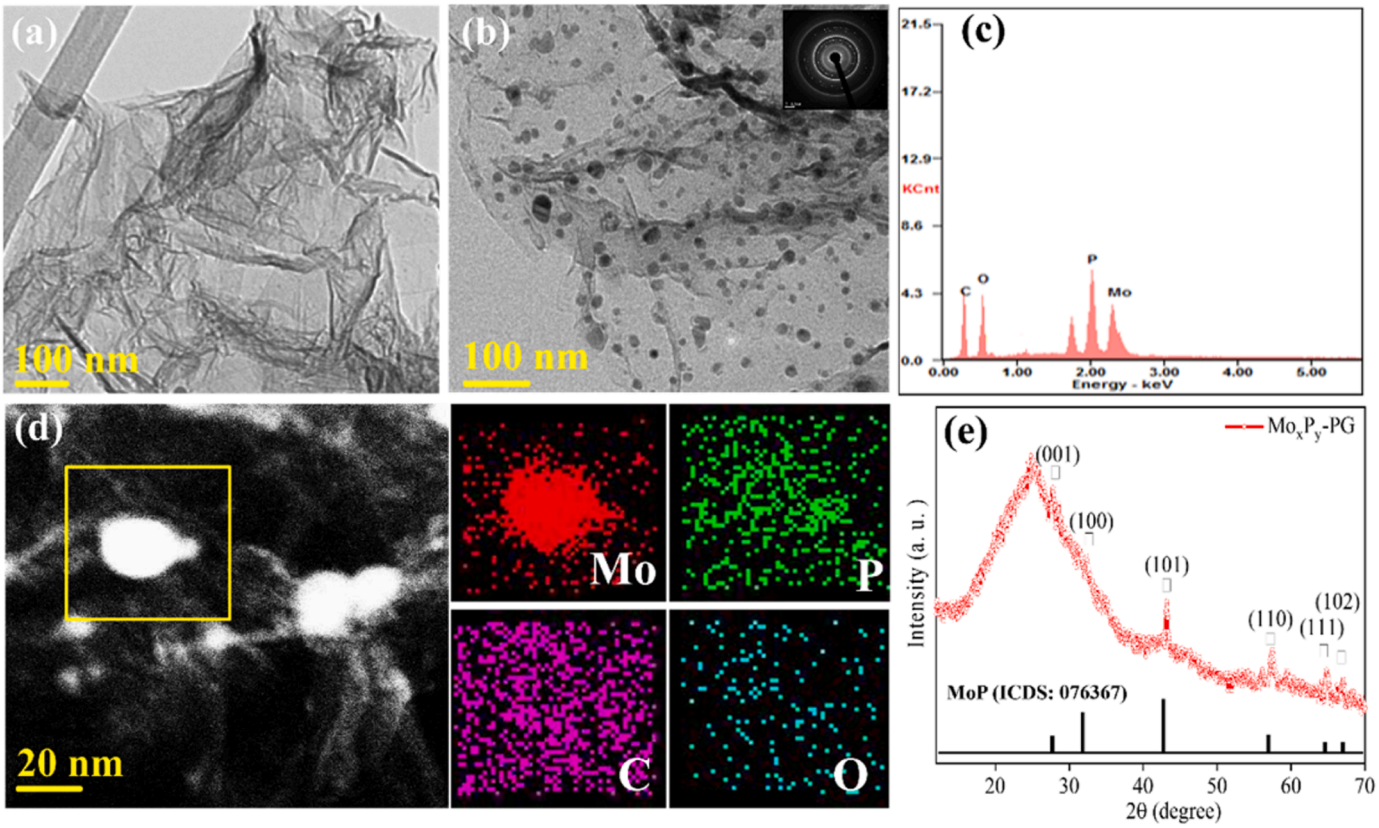

Fig. 3. TEM images of (a) PG and (b) Mo_xP_y-PG materials; (c) EDS spectrum of the Mo_xP_y-PG; (d) Scanning TEM image and EDS color mapping for Mo, P, C, and O; (e) XRD spectra of the Mo_xP_y-PG hybrid material.

constant.

The equation for the conversion from Ag/AgCl reference electrode to (vs. RHE) is shown in Eq. (3):

$$E_{(RHE)} = E_{Ag/AgCl} + 0.059pH + E^{\circ}_{Ag/AgCl} \quad (3)$$

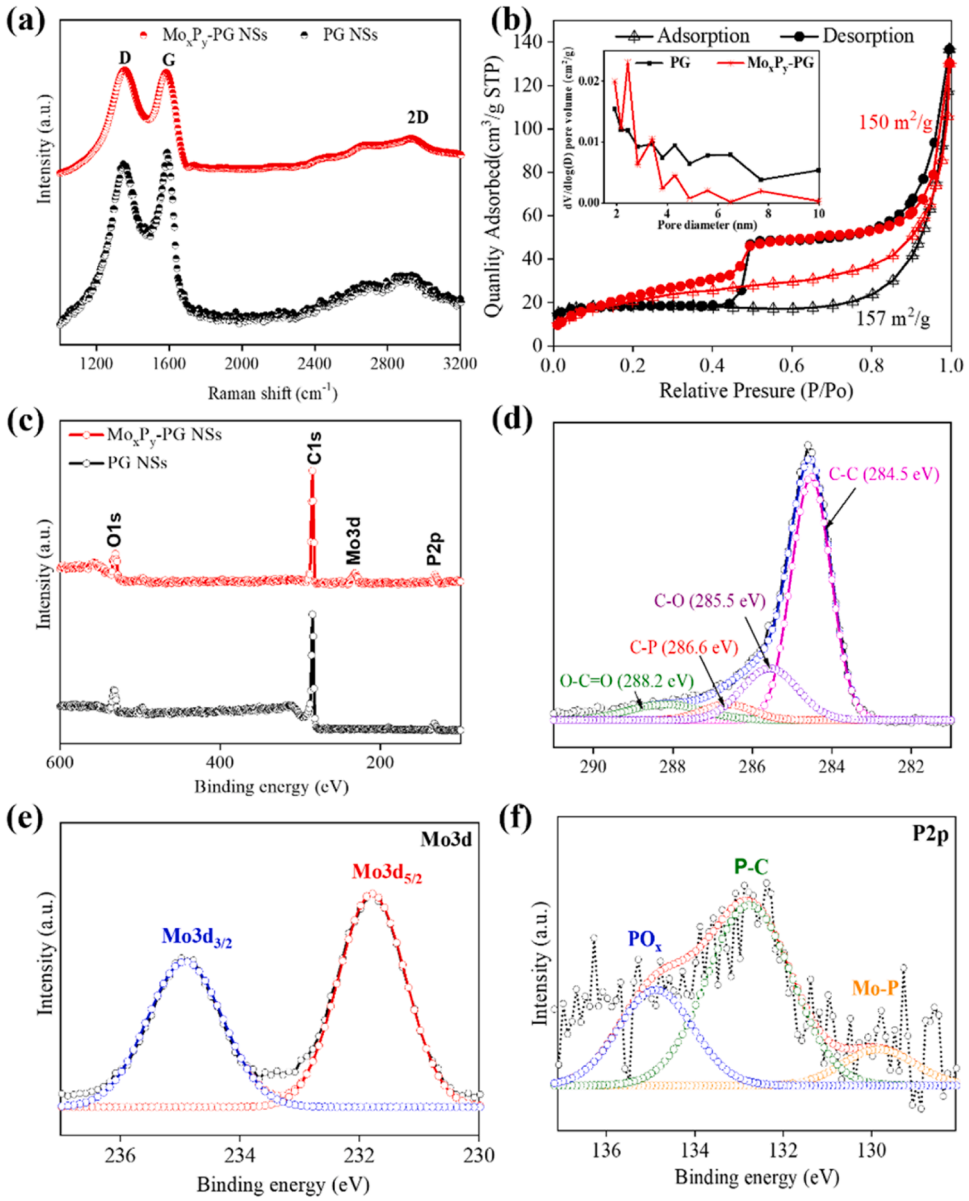

Fig. 4. (a) Raman spectra and (b) BET plots of PG and Mo_xP_y-PG hybrid material. (Inset in Figure b: pore distribution diagrams of hybrid material); (c) The XPS survey spectrum of PG and Mo_xP_y-PG material; High-resolution XPS spectra of (d) C1s, (e) Mo3d, (f) P2p in Mo_xP_y-PG hybrid material.

Where $E°_{Ag/AgCl}$ = 0.1976 V at 25 °C and $E_{Ag/AgCl}$ is the operating potential.

3. Results and discussion

3.1. Morphological properties

Morphological characteristics of the synthesized materials were observed using SEM and TEM analysis. Fig. 2**a-b** show the two-dimensional PG nanosheets having crumpled-like morphology. This phenomenon was attributed to the combined impact of reduction reactions and P-doping effects occurring during a controlled annealing process conducted at a medium temperature. The emergence of a specific P-C bond brought about a notable alteration in bond length, distinguishing it from the typical C–C interactions within the sp^2 features of graphitic graphene. Consequently, this induced scrunches and folds for the graphene structure. Such nano-structural modifications were intriguingly perceived as an open functionalized nanoarchitecture, facilitating effective adhesion, dispersion, and stabilization of active metal nanostructures.

In Fig. 2**c-d**, the morphology of the Mo_xP_y-PG hybrid material is depicted, showcasing the presence of Mo_xP_y nanoparticles, evenly distributed across the surface of the PG nanosheets. The average size of the Mo_xP_y nanoparticle was determined to be 20–30 nm. These small Mo_xP_y nanoparticles were expected to modulate surface chemistry by increasing the number of active sites.

The detailed structures of PG and Mo_xP_y-PG hybrid materials were additionally observed by the TEM study. Fig. 3**a** shows that the synthesized PG was formed as a consecutive layer with numerous wrinkles, originating from the significant number of P heteroatoms doping in the Gr sheet. In addition, the Mo_xP_y nanoparticles were found to have an average size of 25 nm confirmed by the TEM image (Fig. 3**b**). These observations are consistent with the SEM analysis. EDS spectrum was further taken which confirmed the existence of C, P, O, and Mo elements from the Mo_xP_y-PG hybrid structure (Fig. 3**c**). The occurrence of Mo, P, and C elements was further verified by the HAADF-STEM image (Fig. 3**d**) and its consistent EDS color mapping analysis. The spreading of Mo and P was found to be higher at a particular position and thus

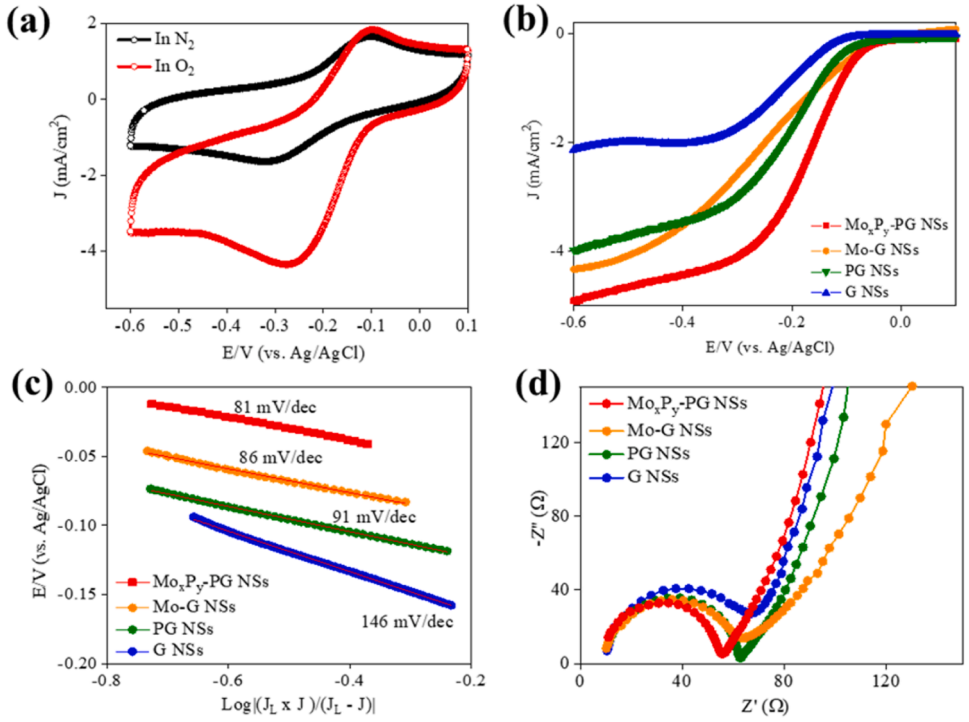

Fig. 5. (a) CV responses of the Mo_xP_y-PG in N_2 and O_2 gas saturated 0.1 M KOH solution at a scan rate of 50 mV/s; (b) LSV curves of materials at a scan rate of 10 mV/s and a rotation speed of 1600 rpm; (c) Tafel responses of materials; (d) EIS analysis of the developed materials.

consistent with the formation of Mo_xP_y nanoparticles. However, the presence of C and P elements throughout the whole scanning area suggests that P-doping must have happened to generate PG. A typical XRD pattern of the Mo_xP_y-PG materials was shown in Fig. 3**e,** which confirmed the creation of crystalline Mo_xP_y over Gr nanosheets and is rational with TEM and EDS achievements. Various peaks appearing at 2θ of 27.79°, 32.3°, 43.16°, 57.47°, 64.79°, and 67.03° can be associated with crystal planes of d(001), d(100), d(101), d(110), d(111), and d (200) in Mo_xP_y nanoparticles, respectively [34]. To further confirm the structure, Raman analysis was done for PG and Mo_xP_y-PG in Fig. 4**a**, which shows the presence of D, G, and 2D bands. From the spectra of two these materials, two peaks related to D band and G band can be observed with strong intensity at 1352 and 1580 cm^{-1}, respectively, while a peak of their 2D band at 2906 cm^{-1} is weak. Now the intensity ratio of these two bands (I_D/I_G) can be found to be higher for Mo_xP_y-PG (1.08) compared to only PG (0.92), suggesting more defects are present in the Mo_xP_y-PG structure, originating from P doping and Mo_xP_y nanoparticle insertion into the graphitic network.

The disordered state within the structure of graphene (Gr) material was anticipated to enhance the hetero-electron transfer ability among the catalyst and host material, as well as between the host material and with current collector within the hybrid structure. This enhancement was projected to augment the reaction kinetics of the catalyst in ORR. Evaluating the specific surface area of the developed materials via nitrogen adsorption-desorption isotherms is essential, as it is a critical determinant of the electrochemical behavior of materials. From Fig. 4**b**, it can be observed that both the PG and Mo_xP_y-PG structures possess IV-type isotherm behavior to produce a BET area of 157 and 150 m^2 g^{-1}, respectively. Moreover, a high volume of nanopores ranging from 2.0 to 8 nm could be found in the structure.

These results suggest that Mo_xP_y-PG hybrid material consists of a high surface area and high volume of nanopores which in turn increase the electroactive catalytic sites in the structure and also the nanopores act as flexible channels for mass transfer. Thus, the catalytic process can be boosted with more active sites and beneficial adsorption of reactant intermediates during the catalysis. The chemical structure and the oxidation statuses of PG and Mo_xP_y-PG hybrid materials were investigated by XPS analysis. Fig. 4**c** indicates that the survey XPS spectra of PG consist of only C1s peak, whereas, Mo_xP_y-PG involves peaks related to C1s, Mo 3d, and P2p at a binding energy of 285, 232, and 132 eV, respectively [35,36]. The high-resolution C1s spectrum of the Mo_xP_y-PG indicates a contribution of different components, including C-C (284.5 eV), C-O (285.5 eV), and O-C═O (288.2 eV) [37]. Furthermore, the presence of the C-P binding energy at 285.5 eV is evident, confirming the effective P-doping within the graphene (Gr) structure. (Fig. 4**d**). The high-resolution Mo3d spectrum can be deconvoluted into two spin-orbit peaks $Mo3d_{5/2}$ and $Mo3d_{3/2}$ at binding energies of 231.8 eV and 234.9 eV, respectively (Fig. 4**e**) [38]. Furthermore, the high-resolution P2p spectrum suggested the formation of Mo_xP_y, C-P, and phosphate species at 129.8, 132.8, and 134.9 eV, respectively (Fig. 4**f**) [39,40]. These observations provided further confirmation for the successful development of Mo_xP_y-PG hybrid material via our synthesis procedure.

3.2. Electrocatalytic ORR activities

The initial approach involved utilizing cyclic voltammetry (CV) analysis to assess the oxygen reduction reaction performance of Mo_xP_y-PG in an alkaline medium solution with both nitrogen- or oxygen-saturated conditions, employing a scan rate of 50 mV s^{-1}. In Fig. 5**a**, a prominent and distinct cathodic peak is observed at approximately −0.274 V in the CV curve acquired under the O_2-saturated condition, while it is absent under the N_2-saturated condition. This observation strongly indicates a favorable catalytic response of the developed hybrids for ORR in an alkaline medium. LSV responses for different developed materials were performed using RDE with a rotating rate of 1600 rpm (Fig. 5**b**). The onset potential of Mo_xP_y-PG was observed at −0.046 V (vs. Ag/AgCl), displaying a more positive value compared to Gr (-0.11 V), PG (-0.08 V), and Mo/Gr (−0.05 V). Likewise, the half-wave potential for Mo_xP_y-PG was registered at −0.17 V (vs. Ag/AgCl) (or +0.854 (vs. RHE)), significantly surpassing the corresponding values for Gr, PG, and Mo/Gr, as well as many hybrid catalysts based on

Table 1
Comparison ORR activity between Mo_xP_y-PG and previous reports.

Catalyst	Electrolyte	Half wave potential (V vs. RHE)	Reference
Mo_xP_y-PG	0.1 M KOH	0.854	This work
3D Co-N-OMMC-0.6	0.1 M KOH	0.83	[41]
$Co_{0.03}$@CoO-N-doped Gr-800	0.1 M KOH	0.81	[42]
3D hollow $NiCo_2O_4$/C	0.1 M KOH	0.68	[43]
3D Nanosheet Co_3O_4 -doped-Gr	0.1 M KOH	0.832	[44]
Co_3O_4/NG	0.1 M KOH	0.74	[45]
C(PANI)/Mn_2O_3	0.1 M KOH	0.784	[46]
SiN-CNTs	0.1 M KOH	0.753	[47]
Fe-N/C-800	0.1 M KOH	0.8	[48]
YS-Co/N-PCMs	0.1 M KOH	0.706	[49]
Fe/N-gCB	0.1 M KOH	0.81	[50]

carbon/graphene materials (Table 1).

In addition, ORR kinetics at the catalyst surface were understood by determining the Tafel slope of catalysts. The Tafel slopes were found to be 146, 91, 86, and 81 mV/dec for Gr, PG, and Mo_xP_y-PG catalysts, respectively (Fig. 5**c**) suggesting the smallest value for Mo_xP_y-PG catalyst and also comparable to the commercially used Pt/C (around 60 mV/dec). This observation indicated an improved oxygen reduction reaction kinetics for Mo_xP_y-PG where electrons are being transferred during the initial oxygen adsorption stage, succeeded by a chemically controlled stage that determines the rate of the reaction. To further study the ORR mechanism, electrochemical impedance spectroscopy (EIS) measurements were conducted for various catalysts, as depicted in Fig. 5**d**. The Nyquist plots of graphene G, PG, Mo-G, and Mo_xP_y-PG exhibited a semicircular segment at high frequency representing charge transfer resistance (R_{ct}) and a linear segment at low frequency representing Warburg (W). R_{ct} value for Mo_xP_y-PG was notably lower than other synthesized materials, signifying its high conductivity in facilitating the ORR reaction.

LSV spectra in O_2-saturated alkaline electrolytes were taken at various rotating rates to understand the catalytic paths for ORR (Fig. 6**a**). Fig. 6**b** displays the corresponding K-L plots of the Mo_xP_y-PG with an overpotential range of −0.60 to −0.40 V. Based on slope values of K-L plots, the number of electrons transported was found to be 2.35–2.5, 3–3.15, 3.57–3.65, and 3.79–3.82 for Gr, PG, Mo-G, and Mo_xP_y-PG, respectively (Fig. 6**c**). The Mo_xP_y-PG material exhibited a notably higher number of electrons transported during the Oxygen Reduction Reaction compared to other materials, indicating a preference for a 4-electron transfer mechanism. This enhanced catalytic performance can be attributed to several key factors: Firstly, the positively charged centers associated with Mo ions within the Mo_xP_y nanoparticles promoted O_2 adsorption. Secondly, the formation of Mo_xP_y nanoparticles induced changes in the electronic structure and surface chemistry, resulting in increased electroactive sites and weakened O-O bonding in O_2.

Thirdly, the presence of active P-C bonding within the graphene structure, due to phosphorus doping effects, significantly contributed to O_2 reduction catalysis. Lastly, the unique nanostructure, with small Mo_xP_y nanoparticles supported by a large area of porous graphene, greatly increased the active center numbers and facilitated electron transfer, thus expediting ORR kinetics. For comparing the catalytic performance of Mo_xP_y-PG with commercial Pt/C material, the LSV (Linear Sweep Voltammetry) curves depicted in Fig. 6**d** indicate that the onset potential of Mo_xP_y-PG closely approximated that of Pt/C, with a negligible difference of only −0.007 V. In addition, the diffusion-limited current density of the Mo_xP_y-PG reached Pt/C, additionally indicating the relatively good electrocatalytic activity of the Mo_xP_y-PG catalyst towards ORR in 0.1 M KOH medium.

To assess the durability of the Mo_xP_y-PG hybrid, an analysis of the amperometry technique was conducted over an extended duration. The chronoamperometric data for MoxPy-PG indicated a marginal decrease in current density, maintaining a remarkable 95% current retention

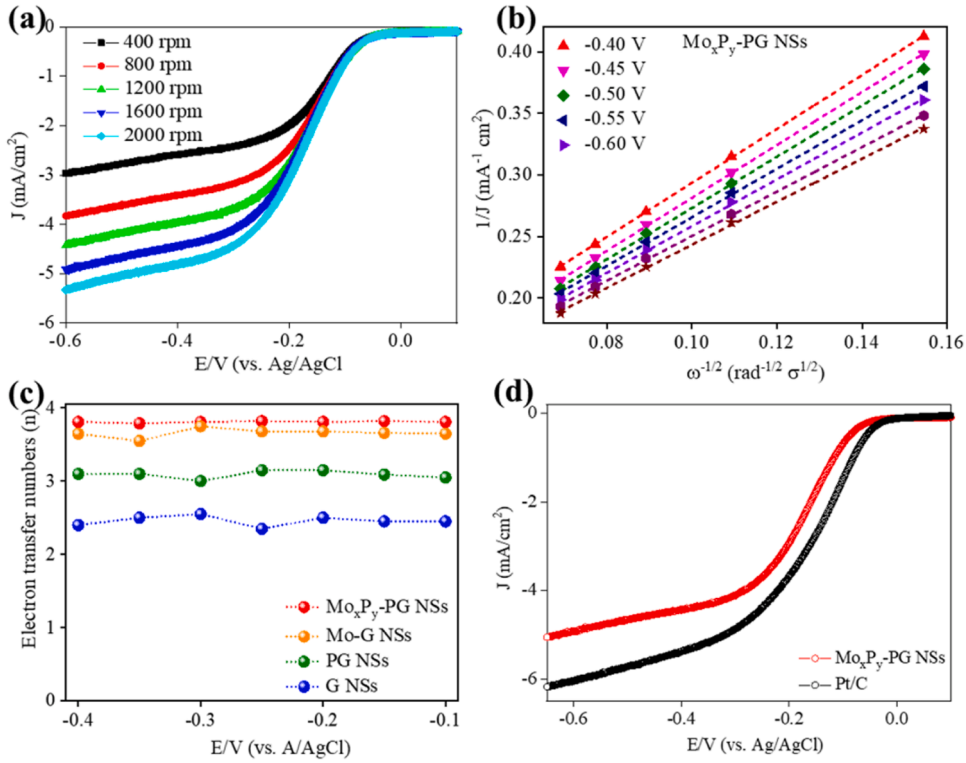

Fig. 6. (a) LSV curves of the Mo_xP_y-PG hybrid material in O_2-saturated 0.1 M KOH solution at a scan rate of 10 mV cm^{-1} and different rotation speeds; (b) The K-L plot of the Mo_xP_y-PG different surveyed potentials; (c) Electron transferred number of materials for ORR; (d) LSVs of the Mo_xP_y-PG and commercial Pt/C material in O_2-saturated 0.1 M KOH solution at a scan rate of 10 mV cm^{-1}.

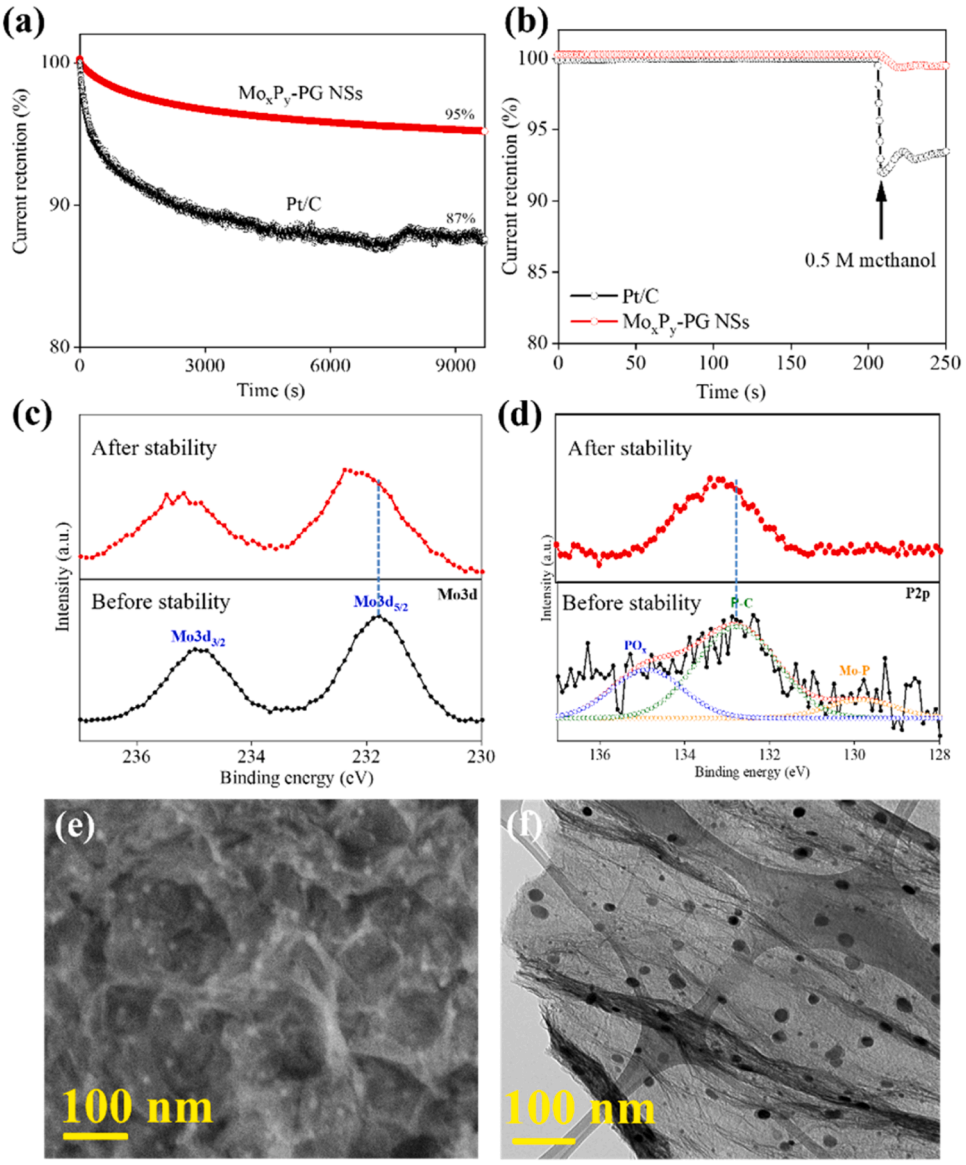

Fig. 7. (a) Chronoamperometric durability of the Mo_xP_y-PG together with commercial Pt/C during a long-term operation; (b) Methanol tolerance ability of the Mo_xP_y-PG and Pt/C; (c-d) XPS spectra of Mo3d and P2p binding energies for pristine and post-ORR Mo_xP_y-PG samples; (e) SEM and (f) TEM images of the post-ORR Mo_xP_y-PG sample.

even after a prolonged operation of 9700 seconds. In contrast, Pt/C exhibited a significantly higher activity loss of approximately 13% (as depicted in Fig. 7**a**), underscoring the superior stability of the Mo_xP_y-PG hybrid material compared to Pt/C. In another regard, the alcohol tolerance of the Mo_xP_y-PG and Pt/C materials was also evaluated. It could be observed that while the current response of the Mo_xP_y-PG presented without significant modulation after adding 0.5 M methanol (Fig. 7**b**), the current response of the Pt/C showed a rapid change due to a serious effect of the methanol oxidation process. In another regard, the structural stability of the post-ORR Mo_xP_y-PG was also investigated by XPS, SEM, and TEM analyses. Fig. 7**c-d** show that the post-ORR Mo_xP_y-PG still possesses Mo3d and P2p binding energies similar to those of the virgin sample, except a positive shift due to surfcae oxidation during long-term operation of the catalyst in aqueous medium. The SEM image in Fig. 7**e** and TEM image in Fig. 7**f** present the good maintaince of the hybrid structure, in which abundance of uniform Mo_xP_y NPs well distribute over surface of the PG.

These accomplishments serve as compelling evidence of the exceptional stability and impressive selectivity exhibited by Mo_xP_y-PG, surpassing that of Pt/C material. This observation suggests that Mo_xP_y-PG holds substantial promise as a cost-effective cathode catalyst for application in alkaline fuel cells.

In order to further understand the catalytic properties of the developed materials, the density of states and free energy were calculated by DFT study with the Vienna Ab initio Simulation Package (VASP). Fig. 8**a** shows different structural models of PG, Mo_xP_y, and Mo_xP_y-PG. These electronic structure analyses indicate that there is an enhancement of DOS near Femi level for the Mo_xP_y-PG as compared to that of the PG, implying the high electronic conductivity of the Mo_xP_y-PG (Fig. 8**b**). In addition, DFT calculations indicate that Mo_xP_y-PG shows the betterfree energy during each ORR step than PG (Fig. 8**c**). Furthermore, the theoretical overpotential of Mo_xP_y-PG is found to be around 0.544 V, samller than that of the PG (1.244 V) (Fig. 8**d**), demonstrating the hybridization between Mo_xP_y and PG can result in a heterostructure with the improved catalytic performance towards ORR.

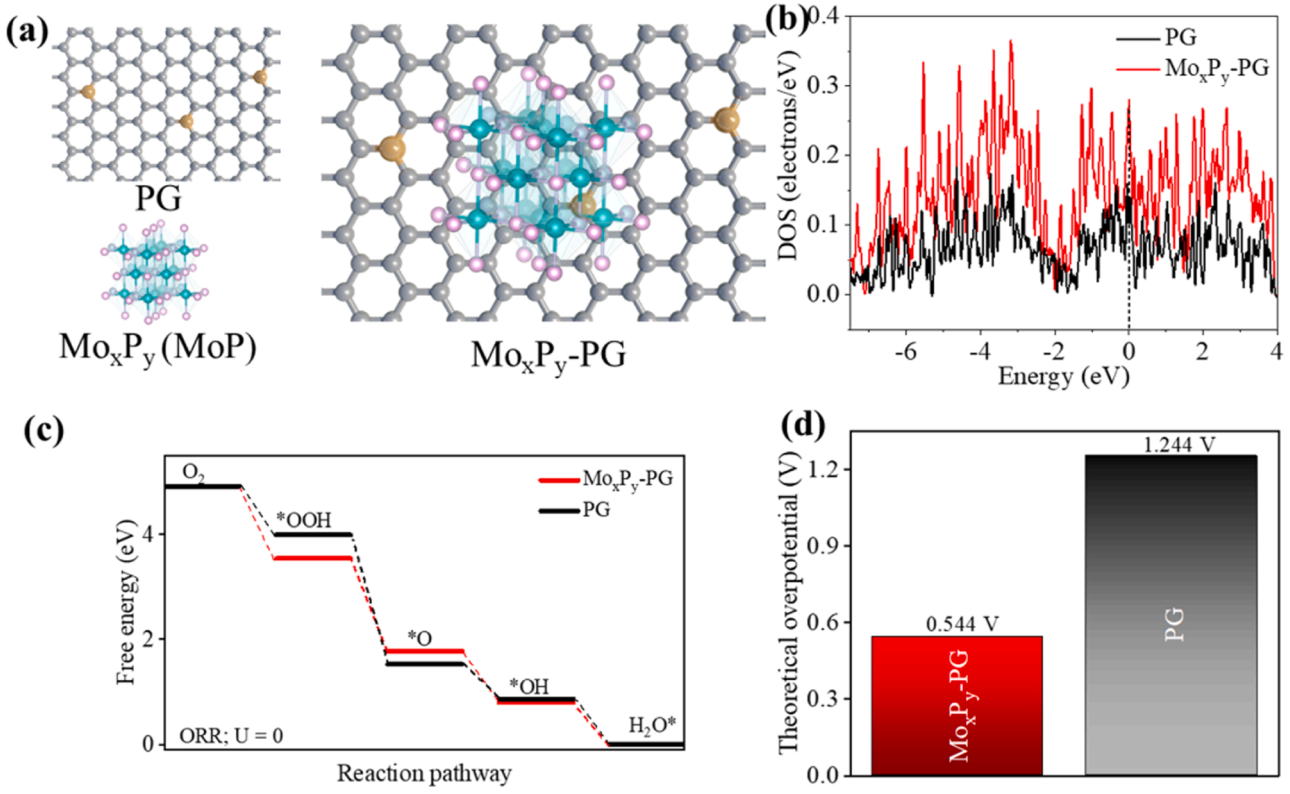

Fig. 8. (a) Structural models for DFT study; (b) DOS of the Mo_xP_y-PG, and PG; (c) Free energy and (d) theoretical overpotential of the Mo_xP_y-PG, and PG for ORR.

4. Conclusion

In this study, we sucessfully sunthesized an effective electrocatalyst based on of Mo_xP_y-PG consisting of nanoscale Mo phosphide nanoparticles uniformly distributed throughout the surface of porous graphene nanosheets. This hybrid material showed significantly low onset potenital of only −0.046 V and a half-wave potential value of roughly −0.17 V (vs. Ag/AgCl) in 0.1 M KOH electrolyte, making it an extremely effective electrocatalyst for the ORR. In addition, the catalyst also outperformed conventional Pt/C catalysts by exhibiting remarkable stability and good tolerance towards the presence of 0.5 M methanol in the alkaline environment. The excellent ORR performance of the devloped Mo_xP_y-PG hybrid can open a new path for the growth of promising highly efficient catalysts for affordable fuel cell technology in energy applications.

CRediT authorship contribution statement

Van Thuan Le: Writing – review & editing, Writing – original draft, Validation, Methodology. **Van Dat Doan:** Writing – review & editing, Validation, Software, Methodology. **L.M. Nguyen:** Writing – review & editing, Validation, Resources, Conceptualization. **H. Van Tran:** Visualization, Investigation. **Vy Anh Tran:** Writing – review & editing, Writing – original draft, Validation, Methodology. **Thu-Thao Thi Vo:** Writing – review & editing, Writing – original draft, Validation, Methodology.

Declaration of Competing Interest

The authors declare that they have no known competing financial interests or personal relationships that could have appeared to influence the work reported in this paper.

Data Availability

Data will be made available on request.

Acknowledgements

The authors acknowledge support from Nguyen Tat Thanh University in Ho Chi Minh City, Vietnam.

References

[1] N. Jung, D.Y. Chung, J. Ryu, S.J. Yoo, Y.E. Sung, Pt-based nanoarchitecture and catalyst design for fuel cell applications, Nano Today 9 (2014) 433–456, https://doi.org/10.1016/j.nantod.2014.06.006.
[2] D. Banham, S. Ye, Current status and future development of catalyst materials and catalyst layers for proton exchange membrane fuel cells: an industrial perspective, ACS Energy Lett. 2 (2017) 629–638, https://doi.org/10.1021/acsenergylett.6b00644.
[3] V.A. Tran, H.H. Do, V.T. Le, Y. Vasseghian, V. Vo, S.H. Ahn, S.Y. Kim, S.-W. Lee, Metal-organic-framework-derived metals and metal compounds as electrocatalysts for oxygen evolution reaction: a review, Int. J. Hydrog. Energy (2021), https://doi.org/10.1016/j.ijhydene.2021.11.063.
[4] S. Sui, X. Wang, X. Zhou, Y. Su, S. Riffat, C. jun Liu, A comprehensive review of Pt electrocatalysts for the oxygen reduction reaction: Nanostructure, activity, mechanism and carbon support in PEM fuel cells, J. Mater. Chem. A Mater. 5 (2017) 1808–1825, https://doi.org/10.1039/C6TA08580F.
[5] H.H. Do, Q.Van Le, T.Van Nguyen, K.A. Huynh, M.A. Tekalgne, V.A. Tran, T.H. Lee, J.H. Cho, M. Shokouhimehr, S.H. Ahn, H.W. Jang, S.Y. Kim, Synthesis of MoSx/Ni-metal-organic framework-74 composites as efficient electrocatalysts for hydrogen evolution reactions, Int. J. Energy Res. (2021), https://doi.org/10.1002/er.6385.
[6] Y.J. Yang, P. Yang, N. Wang, S. Chen, Y. Cheng, M. Liu, C. Jiang, Cobalt nanoparticles with narrow size distribution anchored to flower-like carbon microspheres for enhanced oxygen reduction catalysis, Ionics 28 (2022) 831–838, https://doi.org/10.1007/s11581-021-04353-x.
[7] V.-H. Nguyen, T.-T. Thi Vo, H. Huu Do, V. Thuan Le, T.D. Nguyen, T. Ky Vo, B.-S. Nguyen, T.T. Nguyen, T.K. Phung, V.A. Tran, Ag@ZnO porous nanoparticle wrapped by rGO for the effective CO2 electrochemical reduction, Chem. Eng. Sci. 232 (2021) 116381, https://doi.org/10.1016/j.ces.2020.116381.
[8] V.-H. Nguyen, T.-T. Thi Vo, H. Huu Do, V. Thuan Le, T.D. Nguyen, T. Ky Vo, B.-S. Nguyen, T.T. Nguyen, T.K. Phung, V.A. Tran, Ag@ZnO porous nanoparticle wrapped by rGO for the effective CO2 electrochemical reduction, Chem. Eng. Sci. 232 (2021) 116381, https://doi.org/10.1016/j.ces.2020.116381.

[9] Y. Pei, Y. Cheng, J. Chen, W. Smith, P. Dong, P.M. Ajayan, M. Ye, J. Shen, Recent developments of transition metal phosphides as catalysts in the energy conversion field, J. Mater. Chem. A Mater. 6 (2018) 23220–23243, https://doi.org/10.1039/C8TA09454C.

[10] N.H. Park, J. Kim, Y. Ahn, Fabric-based self-pumping, single-stream microfluidic fuel cell, Electro Acta 446 (2023) 142106, https://doi.org/10.1016/j.electacta.2023.142106.

[11] H.H. Do, M.A. Tekalgne, V.A. Tran, Q.Van Le, J.H. Cho, S.H. Ahn, S.Y. Kim, MOF-derived Co/Co3O4/C hollow structural composite as an efficient electrocatalyst for hydrogen evolution reaction, Fuel 329 (2022), https://doi.org/10.1016/j.fuel.2022.125468.

[12] Y. Zhang, J. Yang, Q. Dong, H. Geng, Y. Zheng, Y. Liu, W. Wang, C.C. Li, X. Dong, Highly Dispersive MoP Nanoparticles Anchored on Reduced Graphene Oxide Nanosheets for an Efficient Hydrogen Evolution Reaction Electrocatalyst, ACS Appl. Mater. Interfaces 10 (2018) 26258–26263, https://doi.org/10.1021/acsami.8b07133.

[13] M. Wei, Y. Luo, C. Jin, J. Sui, Z. Wang, C. Li, R. Yang, MoP nanoflakes as efficient electrocatalysts for rechargeable Li–O_2 batteries, ACS Appl. Energy Mater. (2018) acsaem.7b00299, https://doi.org/10.1021/acsaem.7b00299.

[14] X. Sun, L. Lu, Q. Zhu, C. Wu, D. Yang, C. Chen, B. Han, MoP nanoparticles supported on indium-doped porous carbon: outstanding catalysts for highly efficient CO2electroreduction, Angew. Chem. - Int. Ed. 57 (2018) 2427–2431, https://doi.org/10.1002/anie.201712221.

[15] F. Han, L. Guo, H. Shi, J. Sun, Performance and reaction process of Ba1−xCo0.7Fe0.2Nb0.1O3-δ cathode for intermediate-temperature solid oxide fuel cell, J. Alloy. Compd. 886 (2021), https://doi.org/10.1016/j.jallcom.2021.161158.

[16] J. Su, J. Zhou, L. Wang, C. Liu, Y. Chen, Synthesis and application of transition metal phosphides as electrocatalyst for water splitting, Sci. Bull. (Beijing) 62 (2017) 633–644, https://doi.org/10.1016/j.scib.2016.12.011.

[17] V.A. Tran, H.H. Do, V.T. Le, Y. Vasseghian, V. Vo, S.H. Ahn, S.Y. Kim, S.-W. Lee, Metal-organic-framework-derived metals and metal compounds as electrocatalysts for oxygen evolution reaction: a review, Int. J. Hydrog. Energy 47 (2022) 19590–19608, https://doi.org/10.1016/j.ijhydene.2021.11.063.

[18] M.E. Aristizabal, J. Vega-Castillo, Y.M. Torres, M.D. Sánchez, F. Prado, Stabilization of the cubic perovskite La0.8Pr0.2BaCo2-yO6-δ by introducing Co deficiency and its effect on thermal expansion, electrical conductivity and electrochemical properties, Electro Acta 446 (2023) 142102, https://doi.org/10.1016/j.electacta.2023.142102.

[19] R. Guan, A. Bazylak, Resolving mass transport losses at the catalyst layer of polymer electrolyte membrane fuel cells through semi-empirical modelling, Electro Acta 447 (2023) 142103, https://doi.org/10.1016/j.electacta.2023.142103.

[20] Y.J. Yang, W. Li, Ultrasonic assisted coating of multiwalled carbon nanotubes with NiFe-layered double hydroxide for improved electrocatalytic oxygen reduction, J. Electro Chem. 823 (2019) 499–504, https://doi.org/10.1016/j.jelechem.2018.07.004.

[21] Y.J. Yang, M. Duan, C. Yan, D. Zhao, C. Jiang, X. Duan, X. Song, Facile synthesis of CoFe-LDH/MWCNT/rGO nanocomposite as efficient bifunctional electrocatalysts for oxygen evolution and reduction, J. Electro Chem. 856 (2020) 113697, https://doi.org/10.1016/j.jelechem.2019.113697.

[22] A. Hasanzadeh, A. Khataee, M. Zarei, Y. Zhang, Two-electron oxygen reduction on fullerene C60-carbon nanotubes covalent hybrid as a metal-free electrocatalyst, Sci. Rep. 9 (1) (2019) 13, https://doi.org/10.1038/s41598-019-50155-7.

[23] Y.S. Yun, H. Park, D. Yun, C.K. Song, T.Y. Kim, K.R. Lee, Y. Kim, J.W. Han, J. Yi, Tuning the electronic state of metal/graphene catalysts for the control of catalytic activity: via N- and B-doping into graphene, Chem. Commun. 54 (2018) 7147–7150, https://doi.org/10.1039/c8cc03107j.

[24] K.M. Yam, N. Guo, Z. Jiang, S. Li, C. Zhang, Graphene-based heterogeneous catalysis, Role Graph. (2020).

[25] A.V. Tran, K.H. Shim, T.T. Vo Thi, J.K. Kook, S.S.A. An, S.W. Lee, Targeted and controlled drug delivery by multifunctional mesoporous silica nanoparticles with internal fluorescent conjugates and external polydopamine and graphene oxide layers, Acta Biomater. 74 (2018) 397–413, https://doi.org/10.1016/j.actbio.2018.05.022.

[26] V.A. Tran, T.P. Nguyen, V.T. Le, I.T. Kim, S.-W. Lee, C.T. Nguyen, Excellent photocatalytic activity of ternary Ag@WO3@rGO nanocomposites under solar simulation irradiation, J. Sci.: Adv. Mater. Devices 6 (2021) 108–117, https://doi.org/10.1016/j.jsamd.2020.12.001.

[27] L.M. Rivera, S. Fajardo, M. del, C. Arévalo, G. García, E. Pastor, S-and N-doped graphene nanomaterials for the oxygen reduction reaction, Catalysts 7 (2017), https://doi.org/10.3390/catal7090278.

[28] G. Lemes, D. Sebastián, E. Pastor, M.J. Lázaro, N-doped graphene catalysts with high nitrogen concentration for the oxygen reduction reaction, J. Power Sources 438 (2019), https://doi.org/10.1016/j.jpowsour.2019.227036.

[29] S. Zhuang, H. Singh, B.B. Nunna, D. Mandal, J.A. Boscoboinik, E.S. Lee, Nitrogen-doped graphene-based catalyst with metal-reduced organic framework: chemical analysis and structure control, Carbon N.Y. 139 (2018) 933–944, https://doi.org/10.1016/j.carbon.2018.07.068.

[30] S.A. Giles, Y. Yan, D.G. Vlachos, Effect of substitutionally doped graphene on the activity of metal nanoparticle catalysts for the hydrogen oxidation reaction, ACS Catal. 9 (2019) 1129–1139, https://doi.org/10.1021/acscatal.8b03338.

[31] B. Hu, Y. Yang, W. Cao, X. Wang, C. Zhou, Y. Mao, L. Ge, R. Ran, W. Zhou, Patchy Fe-N-C supported low-loading Pt nanoparticles as a highly active cathode for proton exchange membrane fuel cells, J. Alloy. Compd. 951 (2023), https://doi.org/10.1016/j.jallcom.2023.169867.

[32] T.T.T. Phan, T.T.H. Nguyen, H.T. Huu, T.T. Truong, L.T. Nguyen, V.T. Nguyen, V. A. Tran, T.L. Nguyen, H.L. Nguyen, Hydrothermal synthesis of MoS2/rGO heterostructures for photocatalytic degradation of rhodamine B under visible light, J. Nanomater. 2021 (2021) 9941202, https://doi.org/10.1155/2021/9941202.

[33] Y. Zhang, T. Han, J. Fang, P. Xu, X. Li, J. Xu, C.C. Liu, Integrated Pt2Ni alloy@Pt core-shell nanoarchitectures with high electrocatalytic activity for oxygen reduction reaction, J. Mater. Chem. A Mater. 2 (2014) 11400–11407, https://doi.org/10.1039/c4ta00731j.

[34] S. Wang, J. Wang, P. Li, Z. Wu, X. Liu, N,P-codoped carbon layer coupled with MoP nanoparticles as an efficient electrocatalyst for hydrogen evolution reaction, Materials 11 (2018), https://doi.org/10.3390/ma11081316.

[35] R. Tatara, P. Karayaylali, Y. Yu, Y. Zhang, L. Giordano, F. Maglia, R. Jung, J. P. Schmidt, I. Lund, Y. Shao-Horn, The effect of electrode-electrolyte interface on the electrochemical impedance spectra for positive electrode in Li-Ion battery, J. Electrochem Soc. 166 (2019) A5090–A5098, https://doi.org/10.1149/2.0121903jes.

[36] M. Meng, H. Yan, Y. Jiao, A. Wu, X. Zhang, R. Wang, C. Tian, A "1-methylimidazole-fixation" route to anchor small-sized nitrides on carbon supports as non-Pt catalysts for the hydrogen evolution reaction, RSC Adv. 6 (2016) 29303–29307, https://doi.org/10.1039/C5RA27490G.

[37] X. Yu, Y. Kang, H.S. Park, Sulfur and phosphorus co-doping of hierarchically porous graphene aerogels for enhancing supercapacitor performance, Carbon N.Y. 101 (2016) 49–56, https://doi.org/10.1016/j.carbon.2016.01.073.

[38] J. Cao, X. Zhang, Y. Zhang, J. Zhou, Y. Chen, X. Liu, Free MoS2 nanoflowers grown on graphene by microwave-assisted synthesis as highly efficient non-noble-metal electrocatalysts for the hydrogen evolution reaction, PLoS One 11 (8) (2016) 1, https://doi.org/10.1371/journal.pone.0161374.

[39] Y. Zhao, Y. Zhao, H. Feng, J. Shen, Synthesis of nickel phosphide nano-particles in a eutectic mixture for hydrotreating reactions, J. Mater. Chem. 21 (2011) 8137–8145, https://doi.org/10.1039/c1jm10230c.

[40] M. Kong, H. Song, J. Zhou, Metal–organophosphine framework-derived N,P-codoped carbon-confined Cu_3P nanopaticles for superb Na-ion storage, Adv. Energy Mater. 8 (2018), https://doi.org/10.1002/aenm.201801489.

[41] T. Sun, L. Xu, S. Li, W. Chai, Y. Huang, Y. Yan, J. Chen, Cobalt-nitrogen-doped ordered macro-/ mesoporous carbon for highly efficient oxygen reduction reaction, Appl. Catal. B Environ. 193 (2016) 1–8, https://doi.org/10.1016/j.apcatb.2016.04.006.

[42] G. Zhang, W. Lu, F. Cao, Z. Xiao, X. Zheng, N-doped graphene coupled with Co nanoparticles as an efficient electrocatalyst for oxygen reduction in alkaline media, J. Power Sources 302 (2016) 114–125, https://doi.org/10.1016/j.jpowsour.2015.10.055.

[43] J. Wang, Z. Wu, L. Han, R. Lin, H.L. Xin, D. Wang, Hollow-structured carbon-supported nickel cobaltite nanoparticles as an efficient bifunctional electrocatalyst for the oxygen reduction and evolution reactions, ChemCatChem 8 (2016) 736–742, https://doi.org/10.1002/cctc.201501058.

[44] T. Odedairo, X. Yan, J. Ma, Y. Jiao, X. Yao, A. Du, Z. Zhu, Nanosheets Co3O4 interleaved with graphene for highly efficient oxygen reduction, ACS Appl. Mater. Interfaces 7 (2015) 21373–21380, https://doi.org/10.1021/acsami.5b06063.

[45] M. Zhang, R. Li, X. Chang, C. Xue, X. Gou, Hybrid of porous cobalt oxide nanospheres and nitrogen-doped graphene for applications in lithium-ion batteries and oxygen reduction reaction, J. Power Sources 290 (2015) 25–34, https://doi.org/10.1016/j.jpowsour.2015.04.178.

[46] S. Cao, N. Han, J. Han, Y. Hu, L. Fan, C. Zhou, R. Guo, Mesoporous hybrid shells of carbonized polyaniline/Mn2O3 as non-precious efficient oxygen reduction reaction catalyst, ACS Appl. Mater. Interfaces 8 (2016) 6040–6050, https://doi.org/10.1021/acsami.5b11955.

[47] Z. Liu, X. Fu, M. Li, F. Wang, Q. Wang, G. Kang, F. Peng, Novel silicon-doped, silicon and nitrogen-codoped carbon nanomaterials with high activity for the oxygen reduction reaction in alkaline medium, J. Mater. Chem. A 3 (2015) 3289–3293, https://doi.org/10.1039/C4TA05937A.

[48] W. Niu, L. Li, X. Liu, N. Wang, J. Liu, W. Zhou, Z. Tang, S. Chen, Mesoporous N-doped carbons prepared with thermally removable nanoparticle templates: an efficient electrocatalyst for oxygen reduction reaction, J. Am. Chem. Soc. 137 (2015) 5555–5562, https://doi.org/10.1021/jacs.5b02027.

[49] S. Chao, Q. Cui, K. Wang, Z. Bai, L. Yang, J. Qiao, Template-free synthesis of hierarchical yolk-shell Co and N codoped porous carbon microspheres with enhanced performance for oxygen reduction reaction, J. Power Sources 288 (2015) 128–135, https://doi.org/10.1016/j.jpowsour.2015.04.049.

[50] R. Zhou, S.Z. Qiao, An Fe/N co-doped graphitic carbon bulb for high-performance oxygen reduction reaction, Chem. Commun. 51 (2015) 7516–7519, https://doi.org/10.1039/C5CC00995B.